This is the Pre-Published Version.

This article has been published in a revised form in Journal of Fluid Mechanics [https://doi.org/10.1017/jfm.2016.218]. This version is free to view and download for private research and study only. Not for re-distribution or re-use. © Cambridge University Press 2016.

Dynamics of Internal Jets in the Merging of Two Droplets of Unequal Sizes

Chenglong Tang[1,2,#], Jiaquan Zhao[3,#], Peng Zhang[3,*], Chung K. Law[1,4,*] and Zuohua Huang[2]

[1]Department of Mechanical and Aerospace Engineering, Princeton University, Princeton, New Jersey 08544, USA

[2]State Key Laboratory of Multiphase Flow and Power Engineering, Xi'an Jiaotong University, Xi'an 710049, China

[3]Department of Mechanical Engineering, Hong Kong Polytechnic University, Hong Kong

[4]Center for Combustion Energy, Tsinghua University, Beijing 100084, China

Abstract

The head-on collision, merging, and internal mixing dynamics of two unequal-size droplets were experimentally studied and interpreted, using water, *n*-decane and *n*-tetradecane to identify the distinguishing effects of surface tension and liquid viscosity on the merging and mixing patterns. It is shown that, upon merging of water and n-decane droplets, mushroom-like jets of dissimilar characteristics develop within the merged mass for small and large values of the impact Weber number (*We*), and that such jets are not developed for intermediate values of *We*. Furthermore, such jet-like mixing patterns were not observed for droplets of n-tetradecane, which has smaller surface tension and larger viscosity as compared to water. A regime nomogram relating the Ohnesorge and symmetric Weber numbers is constructed, providing a unified interpretation of the internal mixing patterns. Numerical simulations based on an improved volume-of-fluid method and an adaptive mesh refinement algorithm provide auxiliary diagnoses of the flow fields and the observed phenomena.

Keywords: droplet merging, internal jet, surface tension, viscosity, VOF

# The first and second authors contributed equally to this work.

* To whom correspondence should be addressed. Email addresses: cklaw@princeton.edu (C.K. Law), pengzhang.zhang@polyu.edu.hk (P. Zhang)

1. Introduction

Collision of two droplets in a gaseous environment plays an essential role in many natural and industrial processes, such as raindrop and cloud formation, insecticide spraying, spray painting, and spray combustion in various liquid-fueled engines. For the most symmetrical event, namely the head-on collision between two identical droplets, it has been experimentally (Jiang *et al.* 1992) and theoretically (Zhang & Law 2011) demonstrated that, with increasing impact inertia, the droplets will first merge, then bounce, then merge again, and finally merge followed by further fragmentation with the concomitant production of secondary and even tertiary droplets.

For the collision between two droplets of unequal sizes, studies have been conducted on the global assessment of the merging efficiency. Specifically, Ashgriz & Poo (1990) and Rabe *et al.* (2010) experimentally found that water droplets tend to remain permanently merged as the size differential increases, while Tang *et al.* (2012) demonstrated that this behavior also exists for hydrocarbons. The underlying physics is that viscous dissipation of the excess collisional energy within the merged droplet increases with size disparity so that the droplets can undergo collision with larger Weber numbers without further fragmentation. In addition, Anilkumar *et al.*(1991) experimentally studied the merging and subsequent mixing of initially stationary, low-viscosity droplets of equal and unequal sizes, and found that while there is minimal mixing following merging of equal-size droplets due to symmetry, there is considerable mixing for drops of unequal sizes, with the smaller drop penetrating into the larger drop in the form of a mushroom-like jet. Blanchette *et al.*(2009) simulated the merging of two initially stationary droplets with different surface tensions and observed the jet-pattern mixing within the merged mass even for initially equal-size droplets. Nobari (1993) numerically studied the merging of two initially stationary droplets by using a front tracking method and substantiated the enhanced mixing for small droplet viscosity and large size ratios. Liu *et al*. (2013) performed front-tracking simulation on the merging of unequal-size droplets with Weber numbers up to O(10), and confirmed the crucial role of the surface tension energy of the merged interfaces in forming the jet. Furthermore, the situation of a droplet hitting a liquid pool, which can be treated as a limiting case of unequal-size droplet

collision with the infinite size disparity, has also been extensively studied for vortex ring formation (Thomson & Newall 1885; Hsiao et al. 1988; Shankar & Kumar 1995).

It is noted that in addition to the interest in the fundamental mechanisms governing merging and the subsequent internal mixing when merging is effected, there also exist considerable technological interests in manipulating these processes. As an example, due to the low volatility of gelled hypergolic propellants used in rocket engines (Law 2012), ignition is effected by impinging and merging the bipropellant fuel and oxidizer droplets and jets. The resulting heat release rate would then depend on the internal mixing rate of the merged mass. Another example is the synthesis of novel materials through droplet merging, for which the uniformity or deliberate stratification of the synthesized material would depend on the nature of the internal mixing.

In the present investigation we aim to experimentally identify the morphology and dynamics of the internal jet developed upon merging of two droplets of unequal sizes, particularly the dependence on the impact inertia as well as the physical properties of the fluid, and will show in due course that the nature and occurrence of the jet developed can be highly non-monotonic with respect to the impact inertia. The high-quality experimental images on the droplet collision and jet development event are also expected to be useful in the development and validation of numerical codes for the simulation of discrete gas-liquid two-phase systems. As an attempt, we numerically solved an axi-symmetric formulation of droplet collision by using an improved volume-of-fluid method and an adaptive mesh refinement algorithm. The validated simulation results provide auxiliary information on velocity and pressure fields, which generally are not readily obtained in droplet experiments.

In the following, we will first specify our experimental apparatus and numerical methodology, in Sec. 2. A series of time-resolved droplet collision images with internal flow patterns are shown in Sec. 3, together with the mechanistic interpretation and numerical reproduction of these results.

2. Experimental and Numerical Specifications

2.1 Experimental Apparatus

The schematic of the experimental apparatus is shown in Figure 1. Two droplet streams are independently generated from each glass nozzle by using a circuit to drive a piezoelectric crystal. The sizes of the droplets are adjusted by using nozzles with different apertures. The space uniformity and frequency of the droplets are controlled by the droplet generation circuit. Time-resolved images of droplets were obtained through a stroboscope synchronized with the droplet generation circuit. Droplet pairs are carefully made to collide on the focal plane of the camera, and the sizes of the droplets can be determined from the images at the instant before they start interacting.

The pulse sequence for the phase control of the two droplet streams, the strobe light, and the camera are shown in Figure 2. The basic signal of the system is pulse 1. After careful tuning the width and the amplitude of pulse 1 without/with an appropriate time delay, pulse 5 and 6 are used to drive the two droplet generators to form droplet streams. Additionally, pulse 1 is used to drive the continuous strobe light so that one can see the droplets from a channel of the microscope while adjusting the two droplet generators, which are anchored in three-dimensional positioners, to direct the two droplet streams against each other on the focal plane. By tuning the delay phase of the strobe light, one can see different time sequence of the droplet collision. In order to record the time-resolved images, a Nikon D80 camera is attached to another channel of the microscope, the continuous strobe light is switched to a single shot mode, and the camera flash is synchronized (pulse 8). By flashing the strobe light twice within a pulse period, the camera can record exactly the same droplet with a short phase difference, allowing the determination of the instantaneous droplet velocity.

In the present study, we tuned the delay of the droplet generator and the strobe-light to obtain the images of different droplet pairs, which are assumed to represent the collision processes of the same droplet pair at different time instants. Therefore, an essential requirement of the present experiment is to generate spatially and temporally stable droplets. The adopted methodology including the droplet generation and visualization systems have been sufficiently validated in many previous studies (Jiang *et al.* 1992; Pan *et al.* 2008; Tang *et al.*, 2012) on characterizing the droplet collision outcomes. However, it is extremely difficult to generate identical droplet pairs from two separate nozzles over extended periods of time to characterize droplet internal mixing. As a result, the temporal uncertainty of

collision images is about 0.1ms in the early stages (from droplet contact to merging) while it may be as large as 0.4-0.5ms or 20-30% in the late stages involving droplet oscillation and internal mixing.

In the present experiments the radius of the smaller droplet was fixed at about 100 μm. The size disparity can be changed by using a larger nozzle for the other droplet generator. To visualize the internal mixing pattern upon coalescence of the two droplets, a small amount (less than 0.1% in volume) of a red food coloring dye (ingredients: water, Red 40, modified corn starch, etc.; Ateco Food Coloring, purchased from Amazon) was added in the smaller droplet for water droplet collision. For liquid hydrocarbons, Sudan red II was used because the solubility of the red food coloring dye in hydrocarbons is very small; note that we were not able to identify alternative red dyes with greater solubility in liquid hydrocarbons than Sudan red II. The physical properties of the dyed liquids were tested (The density, viscosity, surface tension of the dyed and un-dyed liquids were tested according to Chinese National Standard GB/T 1884-1992, GB/T 265-1988 and GB/T 6541-1986, respectively.), and results show that such a small amount of dye addition has negligible influence on the liquid properties. To visualize the internal mixing process indicated by the red-dyed fluid, the collision plane should be on the focal plane of the microscope, and a rough surface should be used for the diffuse reflection light to illuminate the focal plane, as shown in Figure 1.

Water, *n*-decane and *n*-tetradecane were used as testing liquids and their viscosities and surface tensions are given in Table 1. The selection of these three fluids provides a controlled study on the effects of surface tension and viscous loss, noting that while water and n-decane have close values of viscosity, their surface tensions are quite different, and while n-decane and n-tetradecane have close values of surface tension, their viscosities are quite different. The collision Weber number is defined as $We_S = 2\rho_l R_S U^2/\sigma$, where ρ_l, R_S, U and σ are respectively the liquid density, droplet radius, relative impact velocity and surface tension, while the subscripts "S" and "L" respectively designate the smaller and larger droplets, with the size ratio given by $\Delta = R_L/R_S$. Because of the importance of viscous dissipation in droplet collision, the Ohnesorge number, $Oh = 16\mu_l/(\rho_l R_S \sigma)^{1/2}$, is adopted to measure the importance of viscous force relative to surface tension. In the present experiments, We_S varies from 5 to 90, Δ from 1.5 to 2.9, and Oh from 0.18 to 0.82. The modified Weber number, We^*=

$We_S\Delta^3/[12(1+\Delta^3)(1+\Delta^2)]$, defined by Tang *et al.* (2012), which measures the relative importance of the total kinetic energy of the droplets in the coordinate system of the center of mass compared to the total surface energy of the droplets before collision, is also used as a parameter accounting for simultaneously the influence of Weber number and the size ratio. It is noted that We^* is exactly the same as the "symmetric Weber number" defined by Rabe *et al.* (2010), if the same definition of size ratio were adopted.

2.2 Numerical Methodology

The computational domain and schematic mesh for the two moving droplets, which are made to collide with each other, are shown in Figure 3. A cylindrical coordinate is established so that the line connecting the centers of mass of the two spherical droplets forms the axial direction. The flow field in both the gas and droplet is treated as incompressible and viscous. The computational domain is an axisymmetric cylinder of $12R_S$ in length and $8R_S$ in radius. The natural oscillation time of the small droplet is $t_{OSC}=(8\rho_l R_s^3/\sigma)^{1/2}$, by which a nondimensional time, $T=t/t_{OSC}$, can be defined. The outflow boundary conditions are specified on all the boundaries expect the axis and further extension of the computational domain will not cause significant change in the results.

It is noted that droplet collision with finite Weber number is a multiple-scale and multiple-physics phenomenon, particularly for those processes involving the intervening gas flow between the impacting droplet surfaces and the subsequent coalescence triggered by the van der Waals force (Zhang & Law 2011). The occurrence of coalescence depends on whether the clearance between the impacting surfaces can reach a critical range of distance which is typically tens of nanometers. Furthermore, the gas-film thickness could vary by 3-4 orders of magnitude during the collision process, and as such poses immense challenges to the computational capacity for spatial resolution. In addition, since the thickness of the gas film can be comparable to the mean free path of gas (Zhang & Law 2011), the rarefied nature of the gas film before coalescence requires numerical artifacts (e.g. adjusting mesh resolution in the present study) in continuum-based numerical methods in order to capture the droplet coalescence and the related phenomena. As a result, quantitatively predictable simulation of droplet coalescence at non-vanishing Weber numbers is not available up to now. The present

computational methodology for simulating droplet collision at non-vanishing Weber numbers is to tune the numerical mesh to capture the droplet deformation during the entire collision process and then use the validated simulation results for more precise and detailed description of the experimental results. The good agreement in terms of droplet mixing in all test cases, to be shown shortly, verifies the adopted computational methodology.

The VOF method adopted by the study has been discussed in detail in (Popinet 2003; Popinet 2009) and implemented in the open source code, Gerris, which has been widely used in many multiphase incompressible flows (Fuster *et al.* 2009; Thoraval *et al.* 2012; Chen *et al.* 2013; Deike *et al.* 2015). In summary, the method is characterized by the combination of the adaptive quad/octree spatial discretization, the geometrical VOF interface representation, the balanced-force/continuum-surface-force surface tension formulation and the height-function curvature estimation. In order to resolve the droplet interface and the internal flow within the droplet, the computational domain was divided into three zones including the gas, the droplet interior and the droplet surface. The mesh for each zone can be adaptively refined to a prescribed level denoted by an integer N, at which the minimum cell size in the zone is of the same order of $R_S/2^N$. We can hence use (N_1, N_2, N_3) to prescribe the refinement levels in all three zones. As an example, Figure 3 shows an illustrative mesh of the refinement levels (5, 6, 7), in which the total number of grid points is 13851and is equivalent to about 50,000 grid points on a fixed, uniform mesh system.

To validate the present numerical methodology, the head-on collision of two unequal-size n-tetradecane droplets was first simulated and compared with the experimental images of Tang *et al.*(2012), as shown in Figure 4. The radius of the small droplet is kept as 100 μm thus the natural oscillation time and Ohnesorge number of the small droplet can be correspondingly obtained. The mesh refinement levels are (5, 10,12) so that the smallest grid size is about $R_S/2^{12}$ and the total number of grid points are 56499, being equivalent to 12.6 million uniform grids. A typical simulation with the above computational domain and mesh generally takes 100 hours of actual time on two Intel Xeon E5-2630 Processors with 24 cores. We selected the computational images that resemble most closely the experimental ones and found that the corresponding times are not identical but are within the experimental uncertainty. The very good agreement between the simulation and experimental results in

terms of the droplet deformation suggest that the adopted VOF method and computer code are suitable for the present problem. It is noted that previous experiments have observed a tiny bubble formed during the droplet coalescence substantiating, albeit indirectly, that the coalescence occurs first at the circular rim. However, the bubble captured in the present VOF simulation is about $0.08R_S$, which is significantly larger than that observed in the experiments (Thoroddsen *et al.* 2003; Bouwhuis *et al.* 2012; Keij *et al.* 2013). To eliminate the possible influence of the unphysically large bubble on the internal flow, we numerically filtered it by following the approach of Liu *et al.* (2013) without causing any significant change to the simulation results, as substantiated in Figure 4.

3. Results and Discussions

3.1 Collision of Water Droplets

Figure 5 shows six sequences of time-resolved images of water droplet collision with increasing impact inertia of the smaller droplet, as represented by its Weber number, We_S. The simulation shows good agreement with the images not only for the droplet deformation but also the internal mixing patterns. The validated simulation provides additional information about the velocity and pressure fields of the phenomena, as shown in Figure 6 for three representative cases. It is seen that, for a relatively small Weber number, We_S=0.47 and $\Delta=1.86$, with the relative impact velocity being 0.37 *m/s*, the droplets do not undergo substantial deformation before they actually come into contact, at t = 0. Upon merging, a transition region in the form of a "neck" is formed around a contact point which connects the two droplets, as shown in Figure 6. The diameter of the neck then increases rapidly up to t = 0.20*ms*, during which no apparent mixing occurs. The merging of the remaining mass into the larger droplet eventually forms a bulge with large curvature and therefore capillary pressure. Subsequently a mushroom-like jet emerges around t=0.67*ms*, after the bulge has completely merged into the larger droplet. Mechanistically, due to the size disparity, the capillary pressure within the smaller droplet exceeds that within the larger droplet by an order of magnitude of $(2\sigma/R_S - 2\sigma/R_L)$. This pressure difference drives the smaller droplet into the larger one through the neck region to form the jet. This internal jet mixing pattern, which we

shall designate as Type I jet, is similar to the observation of Anilkumar *et al.* (1991) in the merging of initially stationary droplets. The same mushroom-like jet is observed for We_s=1.25 and $\Delta=2.09$, formed at t=0.97*ms*.

As the Weber number increases, the mushroom jet-like structure was however not observed, as shown for the cases of We_s = 8.59, $\Delta=2.61$ and We_s = 14.5, $\Delta=2.78$. For the former case the smaller droplet undergoes substantial deformation before it merges with the larger droplet around t=0.17*ms*. Subsequent to the initial merging, the bottom of the smaller droplet is rapidly flattened and an impact crater is formed at t=0.37 and 0.23 *ms* for We_s = 8.59 and 14.5 respectively; note that the camera angle was slightly tilted for these two cases so that the crater surface can be readily observed. Such a crater surface is correctly captured by the present simulation. The relatively large deformation of the droplets indicates that the fluid is spread out to the "ear" area instead of being concentrated along the center line, hence obviating the jet formation, as shown in Figure 6. The images further show that ripples are formed and move towards the "equator" of the larger droplet and then up along the surface of the coalesced mass. The formation of these capillary ripples are related to the strong surface disturbance upon contact of the droplets (Weiss & Yarin 1999) and these ripples were found to play an important role in bubble entrapment during the droplet interaction (Deng *et al.* 2007).

As the Weber number is further increased to We_s = 17.2, another type of mushroom-like jet, the Type II jet, is observed, as seen at t = 2.84*ms*. The mechanism of its formation is different from that for the Type I jet, and has not been observed previously. Specifically, for collisions involving relatively small Weber numbers, it is the surface tension that drives the mass of the small droplet to form the jet structure. For larger Weber numbers, droplet inertia dominates the merging event, as shown by the substantial deformation of the smaller droplet when merging occurs around t=0.07*ms*, followed by the creation of the impact crater which recesses into the larger droplet at t=0.20*ms*. As a result of the large deformation, the fluid originally from the smaller droplet is mostly spread out to the "ear" area and only a small amount of the fluid remains around the center line, as clearly seen in Figure 6. Such a "fluid spreading" is much more significant at higher Weber numbers and is crucial to the subsequent formation of the internal jet. The substantial distortion of the merged mass from spherical

induces strong droplet oscillation, with substantial stretching in the direction of the impact when the Type II jet begins to form at $t = 1.27ms$. The fluid of the larger droplet subsequently tends to "wrap" the dyed fluid as the droplet oscillates. This wrapping process carries the undyed fluids into the center to push the dyed fluid to move forward. As the dyed fluid moves forward, its center is gradually filled with the fluids from the undyed fluids to form a "two-prong" pattern, as seen from the image at $t = 1.87ms$.

3.2 Collision of Hydrocarbon Droplets

Figure 7 shows the collision sequences of n-decane droplets; noting again that Sudan red II in liquid hydrocarbons is not as prominent as the food dye in the water case, although Sudan red II is the most soluble dye that we could locate for liquid hydrocarbons. The images show that the droplet deformation and internal mixing patterns are similar to those of the water droplet collision, with the Type I jet observed at $We_S = 0.84$ and $\Delta = 2.03$. The internal jet can be more readily seen in the enlarged images and the present simulation also reproduced this observation, as shown in Figure 8. The overall response of the hydrocarbon droplets, however, is substantially richer than that of the water droplets in that, as previously observed for the collision between equal-size hydrocarbon droplets in atmospheric pressure (Jiang *et al.* 1992; Pan *et al.* 2008), with increasing collision Weber number (from 0.84 to 2.9 to 18) the collision outcome results in a non-monotonic response of (soft) merging, bouncing, and (hard) merging again. Subsequent to the hard merging, for We_S=18, it is seen that the dyed fluid from the smaller droplet just lodges at the top of the larger droplet and gradually moves down as the droplet oscillates. At We_S=26.7 and 32.0, the Type II jet is again observed, at t=1.35 and 1.42 *ms* respectively, although the images are not as prominent as that for the water droplets, as noted earlier.

Figure 9 shows the collision of n-tetradecane droplets. It is seen that neither Type I jet nor Type II jet is developed within the wide range of Weber numbers, from 0.3 to 63. To explain the absence of the jets, we first note that since n-tetradecane has only a slightly larger surface tension than n-decane, and since surface tension is the driving force for the formation of Type I jet, the absence of the Type I jet for n-tetradecane droplet collisions is then due to its larger viscosity, which is about three times those of water and n-decane. The substantial viscous

dissipation in n-tetradecane droplets then suppresses jet formation, both Type I and Type II. We also note that, similar to n-decane, bouncing was also observed for n-tetradecane droplet collision, as it should be, while the deformation process of the coalesced mass is also similar to those of water and n-decane.

Another interesting phenomenon was observed for We_s= 63.0 and Δ= 2.85. Because of the high impact inertia, an obvious impact crater was observed at t = 0.27 *ms*, with the sidewall of the crater appearing to close in at t = 0.33*ms*. As a result, some gas charge would be trapped in the merged mass if the side wall closes before the crater completely recedes. This gas charge entrapment was consistently observed, as indicated by the dashed arrows in Fig. 10, with the trapped gas charge appearing as a filament instead of a bubble.

3.3 Regime nomogram of internal mixing pattern

Different internal mixing patterns in the parameter space of 1/Oh (instead of Oh for mathematical convenience) and We* are illustrated in Fig. 11. The selection of these parameters is based on the following considerations. First, internal mixing is observed to be suppressed in highly viscous droplets. As such, the Ohnesorge number, Oh, representing the relative importance of viscosity compared to surface tension, with n-tetradecane having the largest Oh while water the smallest one, is an important parameter. Second, the facilitation of internal mixing with increasing size ratio is physically straightforward in that the jet-like mixing is absent for equal-size droplet due to symmetry while it always occurs in the limiting case of droplet impacting a liquid pool, which has an infinite size ratio. Consequently, We* or the symmetric Weber number (Rabe *et al.* 2010) is the physically meaningful combination to include the influence of both Weber number and size disparity.

Figure 11 shows that there exists a minimum 1/Oh below which jet-like mixing is absent, as least within the range of *We** investigated. With increasing 1/Oh, jet-like mixing emerges. The phenomenon, however, is further enriched by its nonmonotonic variation with the impact Weber number in that not only the jet is Type I for the low *We**, soft merging, and Type II for the high *We*,* hard merging, but these two jet-formation regimes are also separated by a *We** regime in which jet is not formed. Mechanistically, for small *We** as a result of either

sufficiently small We_S or sufficiently large Δ, 1/Oh is the controlling parameter for Type I jet such that decreasing viscosity promotes jet formation. At higher We^*, the dominating factor is the inertia of the impacting droplets, which favors penetration of the smaller droplet into the larger one to form the jet-like mixing pattern, while viscous dissipation should be sufficiently small to facilitate the penetration. Furthermore, it is also seen that the transition Weber numbers between the Type I jet regime and the no-jet regime increase with 1/Oh, while those between the no-jet regime and the Type II jet regime decrease with 1/Oh, resulting in a shrinking, albeit gradual, no-jet regime with increasing 1/Oh.

We finally note that while mixing can occur for equal-size droplet with variable surface tension (Blanchette *et al.* 2009; Blanchette *et al.* 2010) and non-Newtonian fluids (Sun *et al.* 2015a; Sun *et al.* 2015b), and that pinch-off can also occur for droplet impacting a liquid pool at sufficiently large Weber numbers (Thomson & Newall 1885; Hsiao *et al.* 1998) or unequal-size droplet collision with sufficient large size ratio (Blanchette & Bigioni 2009), these auxiliary phenomena do not affect the central tenant of the present discussion, and can be grafted into the present regime nomogram for a more detailed texture.

3.4 Long-term Dynamics of Internal Mixing

The evolution of the jet-like internal mixing patterns is of technological interest in manipulating the mixing process in many applications. For example, the long-term dynamics of the droplet mixing in merged bipropellant fuel and oxidizer droplets affects the subsequent liquid-phase reactions and gas-phase ignition (Solomon *et al.* 2013). However, corresponding experimental data are not available in the present study due to the following technical difficulties. First, droplet collision occurs on the vertical focal plane and the view of the camera which is connected to a microscope is limited. As a result, the droplet will move out of the view under gravity at longer times. While reducing the magnification factor of the microscope can capture the droplet in the camera for a longer time, it deteriorates the quality of the images showing the droplet internal mixing. Second, the accuracy of the time delay between the strobe-light and the droplet generator is reduced because the droplet pairs become less stable after coming out from the droplet nozzle for a longer time.

In consideration of these technical difficulties in characterizing the long-term dynamics of internal mixing experimentally, we conducted simulations of water droplet collision for a sufficiently long time up to eight characteristic oscillation times. Figure 12 shows the calculated mixing patterns for the fixed Δ=2.43 and Oh=0.19 but with varying We_S and hence We*. Figure 13 shows the calculated mixing patterns for the fixed We_S =17.2 and Oh=0.19 but with varying Δ and hence We*. Both figures share the same case of, which has been shown in Figure 5. Furthermore, all the cases reported in the figures use the same mesh for consistency. Consequently, the results shown in Figures 12 and 13 can be considered as extensions of the experimental study by varying one parameter at a time and for a longer time.

To quantitatively describe the internal mixing within the merged droplet, a mixing index *M* varying between 0 and 1 can be defined as follow (Yeh *et al.* 2013),

$$M - \frac{\int_V |C - C_0| S(f-1) dV}{\int_V |C_0 - C_\infty| S(f-1) dV}$$

$$C - \frac{|\emptyset - 0.5|}{0.5} C_0, C_0 - \begin{Bmatrix} 0, \emptyset = 0 \\ 1, \emptyset > 0 \end{Bmatrix}, C_\infty - \frac{1}{1+\Delta^3}$$

where C, C_0 and C_∞ are the distribution functions of the time-dependent "concentration" of the small droplet liquid in the merged mass, in the unmixed droplet, and in the fully mixed mass; Φ is the spatially and temporally varying dye function, which is defined as 1 in the small droplet and 0 in the larger droplet; and f is the VOF function, which is equal to 0 in the gas phase and 1 in the liquid phase. The Heaviside step function $S(f-1)$ ensures that the integration is only for the droplets. The calculated mixing indices are shown in each images in Figures 12 and 13 and summarized in Figure 14.

Figures 12 and 13 show that the jets have been sufficiently developed during the reported times of experiment. The subsequent event is characterized by a moderate variation of the jet shape due to the droplet oscillation, which will be eventually damped down by the viscous dissipation. Figure 12 again shows the expected phenomena that the jet-like mixing patterns are apparent at sufficiently small and large Weber numbers, while they become less distinct at intermediate Weber numbers. The corresponding long-term behavior of the mixing indices, as shown in Figure 14 (a), quantitatively verify this observation as the mixing indices after T=4

show non-monotonic variation with the Weber number (either We_S or We*). In addition, Figure 13 shows that the internal mixing is enhanced by increasing the size ratio, which can be also seen in Figure 14 (b) as the mixing indices after T=4 vary monotonically with We*, which decreases with increasing Δ.

4. Concluding remarks

Motivated by the interest to facilitate mixing of two impacting droplets, we have experimentally identified and numerically reproduced the influence of the impact inertia and the physical properties of the fluid on the merging tendency and the subsequent mixing characteristics. In particular, we have shown that for liquids with large surface tension and small viscosity such as water and n-decane, mixing is facilitated by the development of distinctively different jet patterns for small and large values of the impact Weber number, and the absence of such jets and thereby effective mixing for intermediate values. Furthermore, jet formation is also inhibited for liquids with large viscosities that reduce the impact inertia. The regime nomogram classifying the mixing responses is expected to facilitate further optimization. To explain the observed phenomena, we attribute the formation of Type I jet at small Weber numbers to the merging of a liquid "bulge" formed during the coalescence of the small droplet into the larger one at the contact point around the central line. At higher Weber numbers, the droplets undergo substantial deformation before coalescence so that the droplets merge at significantly flattened surface, which suppresses the concentration of the droplet momentum along the central line and hence the jet formation. However, at even higher Weber numbers, the large droplet deformation results in the mass of the small droplet being first spread out away from the impact crater. The subsequent droplet oscillation, particularly the droplet stretching in the direction of the impact, carries the mass of the small droplet into the larger droplet to form the Type II jet, which is centrally hollow and is therefore different from the Type I jet. It is also noted that the present interpretations of the formation mechanisms for Type I and Type II jets are largely mechanistic and phenomenological. Numerical simulation based on improved VOF method with adaptive mesh refinement algorithm could further resolve the interface evolution upon droplet merging and the subsequent mixing process.

Acknowledgement

CT was a visiting student at Princeton University where the experiment was performed. The subsequent work at the Xi'an Jiaotong University was supported by the National Science Foundation of China (51206131), while that at the Hong Kong Polytechnic University by the Hong Kong RGC/GRF (PolyU/15221714) and SRFDP & RGC ERG Joint Research Scheme (M-PolyU509/13). The simulations were conducted using the resources of the High Performance Cluster Computing Centre, Hong Kong Baptist University.

References

ANILKUMAR, A. V., LEE, C. P. & WANG, T. G. 1991 Surface-tension-induced mixing following coalescence of initially stationary drops. *Phys. Fluids A-FLUID DYNAMICS* **3,** 2587-2591.

ASHGRIZ, N. & POO, J. Y. 1990 Coalescence and separation in binary collisions of liquid drops. *J. Fluid Mech.* **221,** 183-204.

BLANCHETTE, F. 2010 Simulation of mixing within drops due to surface tension variations. *Phys Rev Lett* **105,** 074501.

BLANCHETTE, F. & BIGIONI, T. P. 2009 Dynamics of drop coalescence at fluid interfaces. *J. Fluid Mech.* **620,** 333-352.

BLANCHETTE, F., MESSIO, L. & BUSH, J. W. M. 2009 The influence of surface tension gradients on drop coalescence. *Phys. Fluids* **21,** 072107.

BOUWHUIS, W., VAN DER VEEN, R. C. A., TRAN, T., KEIJ, D. L., WINKELS, K. G., PETERS, I. R., VAN DER MEER, D., SUN, C., SNOEIJER, J. H. & LOHSE, D. 2012 Maximal air bubble entrainment at liquid-drop impact. *Phys. Rev. Lett.* **109,**

CHEN, X. D., MA, D. J., YANG, V. & POPINET, S. 2013 High-fidelity simulations of impinging jet atomization. *Atomization Sprays* **23,** 1079-1101.

DEIKE, L., POPINET, S. & MELVILLE, W. K. 2015 Capillary effects on wave breaking. *J. Fluid Mech.* **769,** 541-569.

DENG, Q., ANILKUMAR, A. V. & WANG, T. G. 2007 The role of viscosity and surface tension in bubble entrapment during drop impact onto a deep liquid pool. *J. Fluid Mech.* **578,** 119-138.

FUSTER, D., AGBAGLAH, G., JOSSERAND, C., POPINET, S. & ZALESKI, S. 2009 Numerical simulation of droplets, bubbles and waves: State of the art. *Fluid Dyn. Res.* 41, 065001.

HSIAO, M. Y., LICHTER, S. & QUINTERO, L. G. 1988 The critical weber number for vortex and jet formation

for drops impinging on a liquid pool. *Phys. Fluids* **31,** 3560-3562.

JIANG, Y. J., UMEMURA, A. & LAW, C. K. 1992 An experimental investigation on the collision behavior of hydrocarbon droplets. *J. Fluid Mech.* **234,** 171-190.

KEIJ, D. L., WINKELS, K. G., CASTELIJNS, H., RIEPEN, M. & SNOEIJER, J. H. 2013 Bubble formation during the collision of a sessile drop with a meniscus. *Phys. Fluids* **25**, 082005.

LAW, C. K. 2012 Fuel options for next-generation chemical propulsion. *AIAA J.* **50,** 19-36.

LIU, D., ZHANG, P., LAW, C. K. & GUO, Y. C. 2013 Collision dynamics and mixing of unequal-size droplets. *Int. J. Heat Mass Tran.* **57,** 421-428.

NOBARI, M. R. 1993 Numerical simulations of drop collisions and coalescence. Ph. D Thesis, The University of Michigan.

PAN, K. L., LAW, C. K. & ZHOU, B. 2008 Experimental and mechanistic description of merging and bouncing in head-on binary droplet collision. *J Appl. Phys.* **103,** 064901.

POPINET, S. 2003 Gerris: A tree-based adaptive solver for the incompressible euler equations in complex geometries. *J. Comput. Phys*. **190,** 572-600.

POPINET, S. 2009 An accurate adaptive solver for surface-tension-driven interfacial flows. *J. Comput. Phys.* **228,** 5838-5866.

RABE, C., MALET, J. & FEUILLEBOIS, F. 2010 Experimental investigation of water droplet binary collisions and description of outcomes with a symmetric weber number. *Phys. Fluids* **22,** 047101.

SHANKAR, P. N. & KUMAR, M. 1995 Vortex rings generated by drops just coalescing with a pool. *Phys. Fluids* **7,** 737-746.

SOLOMON, Y., DEFINI, S. J., POURPOINT, T. L. & ANDERSON, W. E. 2013 Gelled monomethyl hydrazine hypergolic droplet investigation. *J.Propu. Power***29,** 79-86.

[a]SUN, K., WANG, T., ZHANG, P. & LAW, C. K. 2015 Non-Newtonian flow effects on the coalescence and mixing of initially stationary droplets of shear-thinning fluids. *Phys. Rev. E* **91,** 023009.

[b]SUN, K., ZHANG, P., LAW, C. K. & WANG, T. 2015 Collision dynamics and internal mixing of droplets of non-newtonian liquids. *Phys. Rev. Appl.* **4,** 054013.

TANG, C., ZHANG, P. & LAW, C. K. 2012 Bouncing, coalescence, and separation in head-on collision of unequal-size droplets. *Phys. Fluids* **24,** 022101.

THOMSON, J. J. & NEWALL, H. 1885 On the formation of vortex rings by drops falling into liquids, and some allied phenomena. *Proc. R. Soc. London* **39,** 417-436.

THORAVAL, M. J., TAKEHARA, K., ETOH, T. G., POPINET, S., RAY, P., JOSSERAND, C., ZALESKI, S. & THORODDSEN, S. T. 2012 Von karman vortex street within an impacting drop. *Phys. Rev. Lett*. **108,** 264506.

THORODDSEN, S. T., ETOH, T. G., & TAKEHARA, K. 2003 Air entrapment under an impacting drop. *J. Fluid. Mech*. **478,** 125-134.

WEISS, D. A., YARIN, A. L. 1999 Single drop impact onto liquid films: Neck distortion, jetting, tiny bubble entrainment, and crown formation. *J. Fluid. Mech.* **385,** 229-254.

YEH, S. I., FANG, W. F., SHEEN, H. J., & YANG, J. T. 2013 Droplets coalescence and mixing with identical and distinct surface tension on a wettability gradient surface. *Microfluid. Nanofluid.* **14,** 785-795.

ZHANG, P. & LAW, C. K. 2011 An analysis of head-on droplet collision with large deformation in gaseous medium. *Phys. Fluids* **23,** 042102.

Table 1. Properties of tested liquids

Liquids	Surface tension, □	Viscosity, □	Density, □
	10^{-2}N/m	10^{-3}Ns/m^2	10^3kg/m^3
Water	7.29	0.89	1.0
N-decane	2.38	0.85	0.73
N-tetradecane	2.65	2.03	0.76

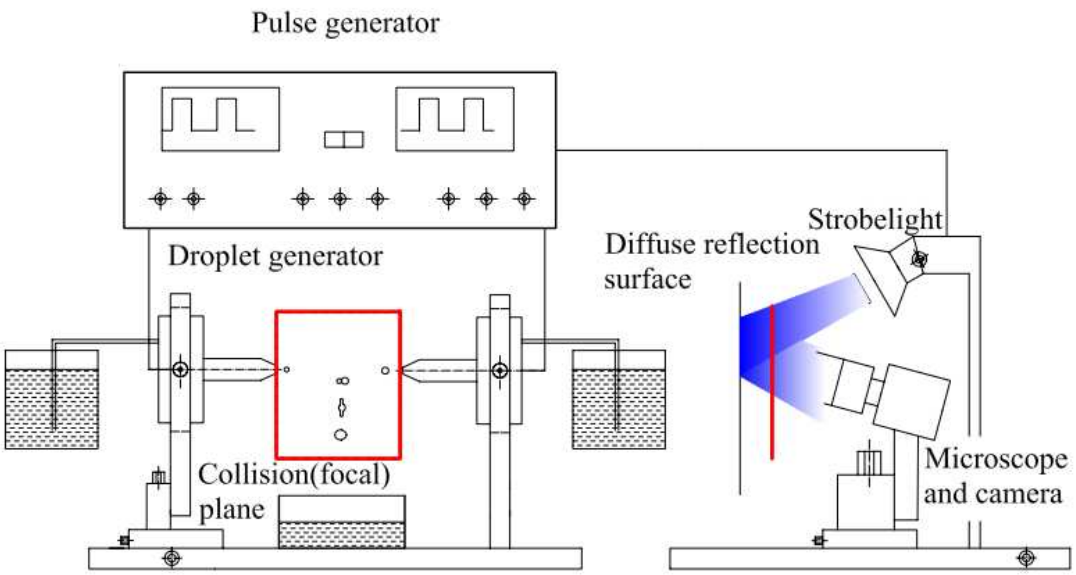

Figure 1 Schematic of the experimental apparatus. The front-view of the collision plane captured by the camera is shown in the rectangular, the corresponding side view is shown on the right-hand-side of the figure for its relative position with respect to the camera and strobelight.

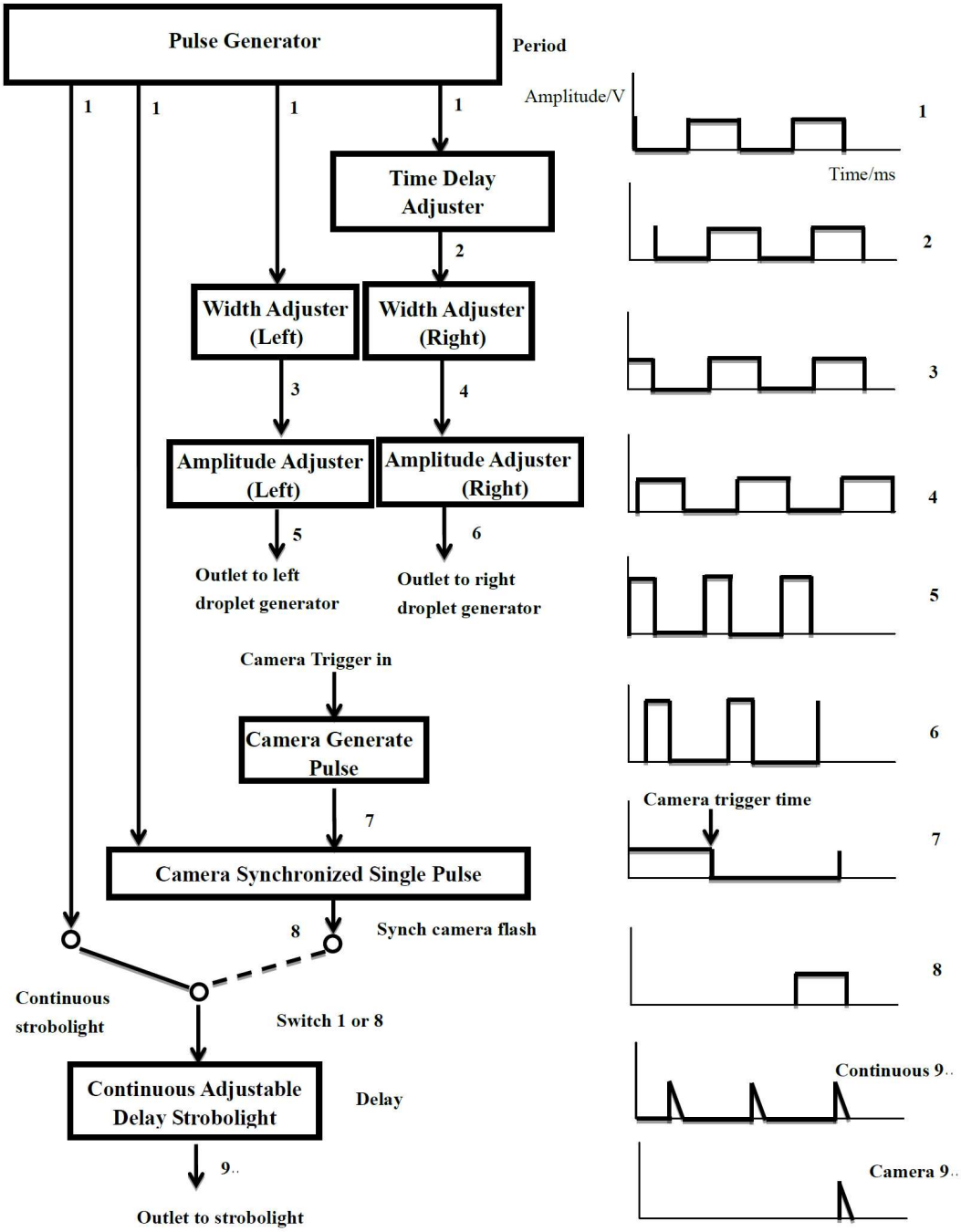

Switch 1: Continuous strobolight illuminate the view for experimenter to adjust the pulse for droplet generators; by tuning the delay of pulse 9, collision at different phases are observed

Switch 8: When the collision at a fixed delay is ready, camera synchronized single pulse triggers the flash and the collision image at this specific delay is recorded

Figure 2. Pulse sequences and synchronization of signals

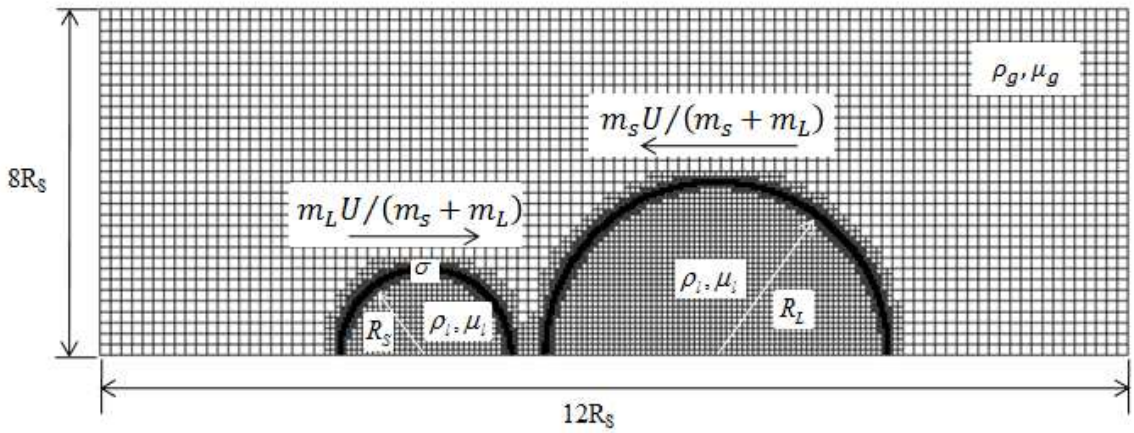

Figure 3. Computational domain and schematic adaptive mesh for the VOF simulation of unequal-size droplet collision.

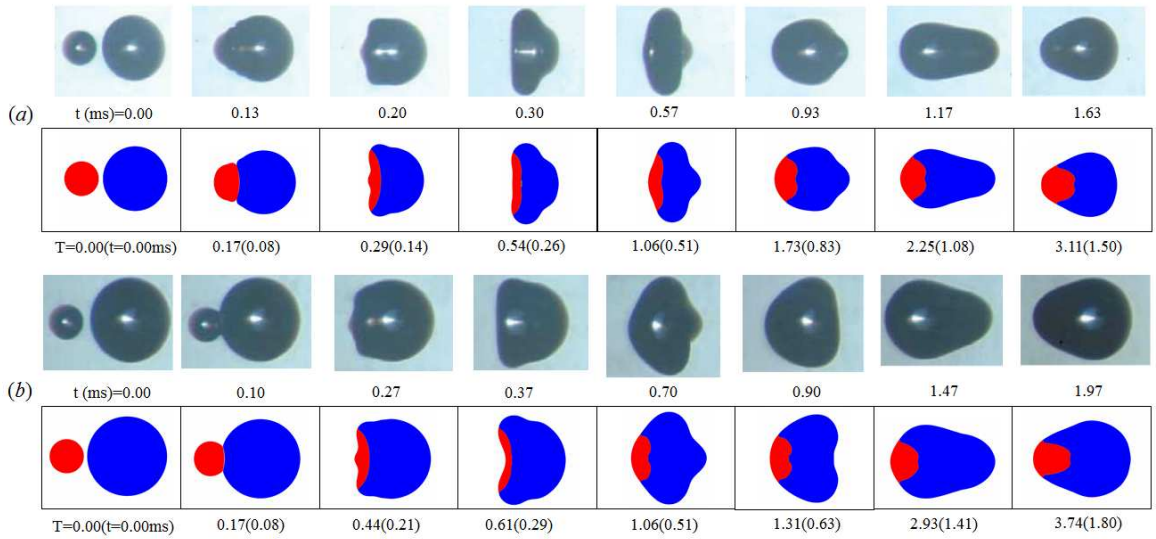

Figure 4. Head-on collision of two n-tetradecane droplets for: (a) We_S =17.6, Δ=1.87 and (b) We_S =16.5, Δ=2.33. The oscillation time and the Ohnesorge number of the smaller droplet are t_{OSC}=0.48ms and Oh=0.82, respectively. Experimental images are adapted from Tang *et al.* (2012).

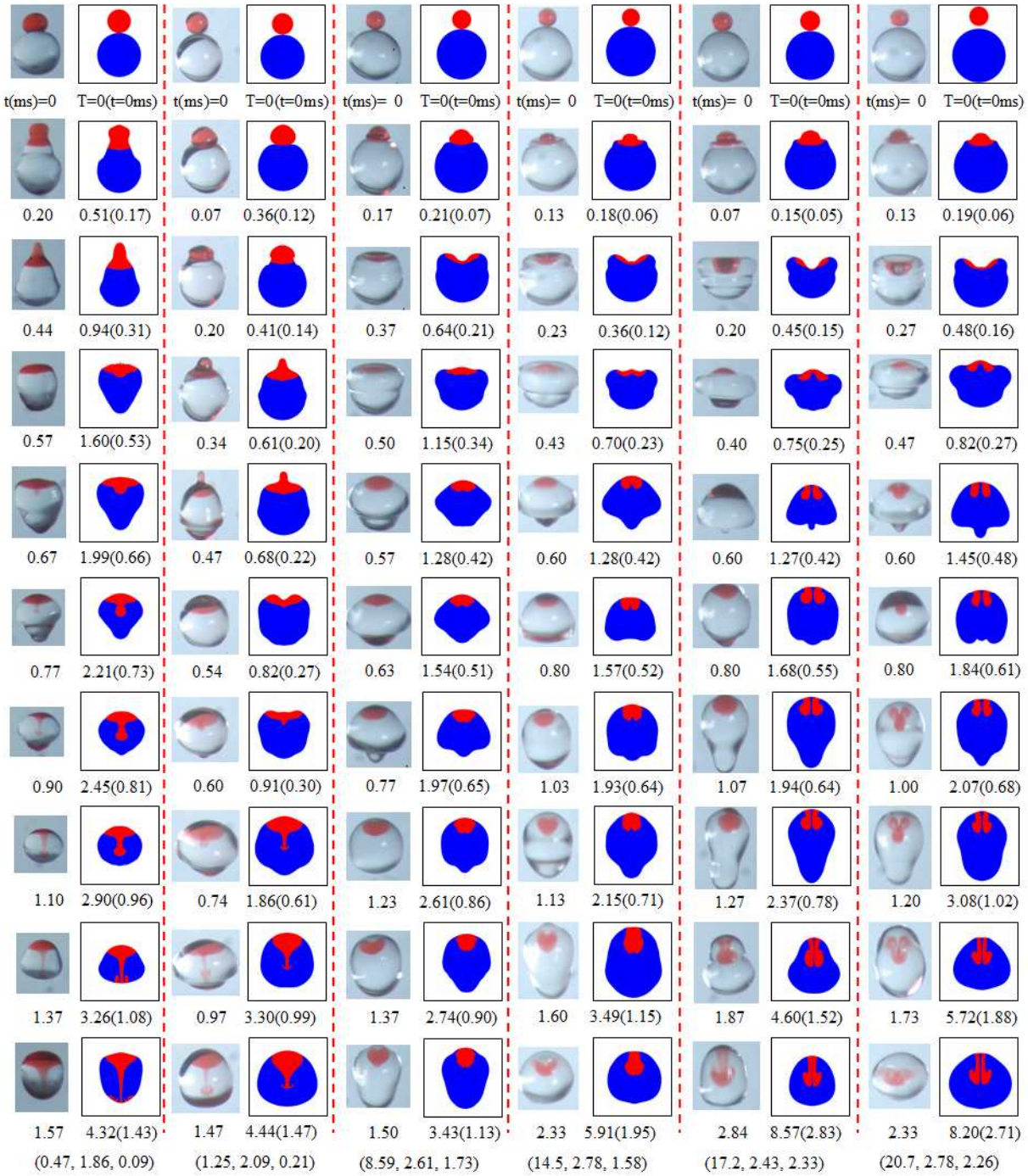

Figure 5. Mixing pattern during collision of water droplets for (We_S, Δ, We^*). The oscillation time and the Ohnesorge number of the smaller droplet are t_{OSC}=0.33ms and 0.19, respectively.

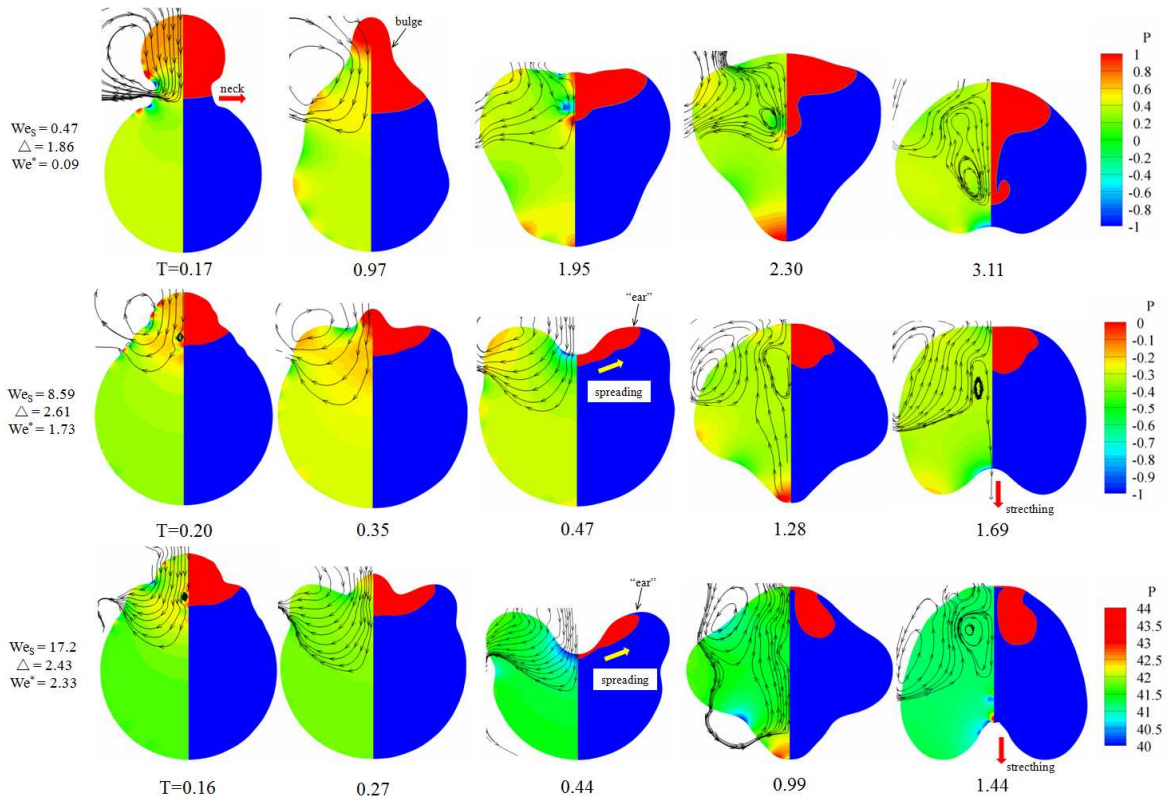

Figure 6. Streamlines, pressure field and mixing pattern during collision of water droplets. The oscillation time and the Ohnesorge number of the smaller droplet are t_{OSC}=0.33ms and Oh=0.19, respectively.

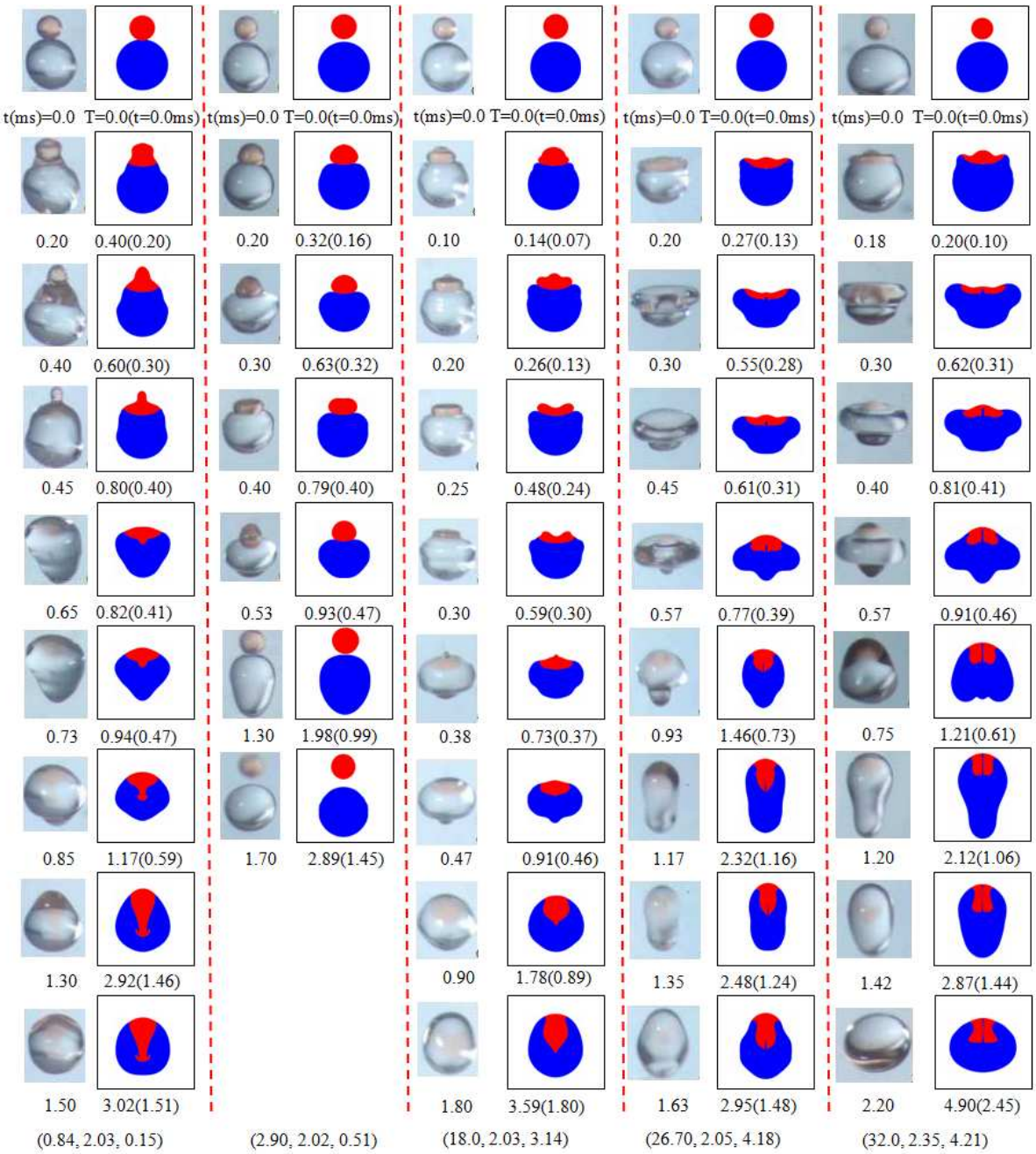

Figure 7. Mixing pattern during collision of n-decane droplets for (We_S, Δ, We^*). The oscillation time and the Ohnesorge number of the smaller droplet are t_{OSC}=0.50ms and 0.35, respectively.

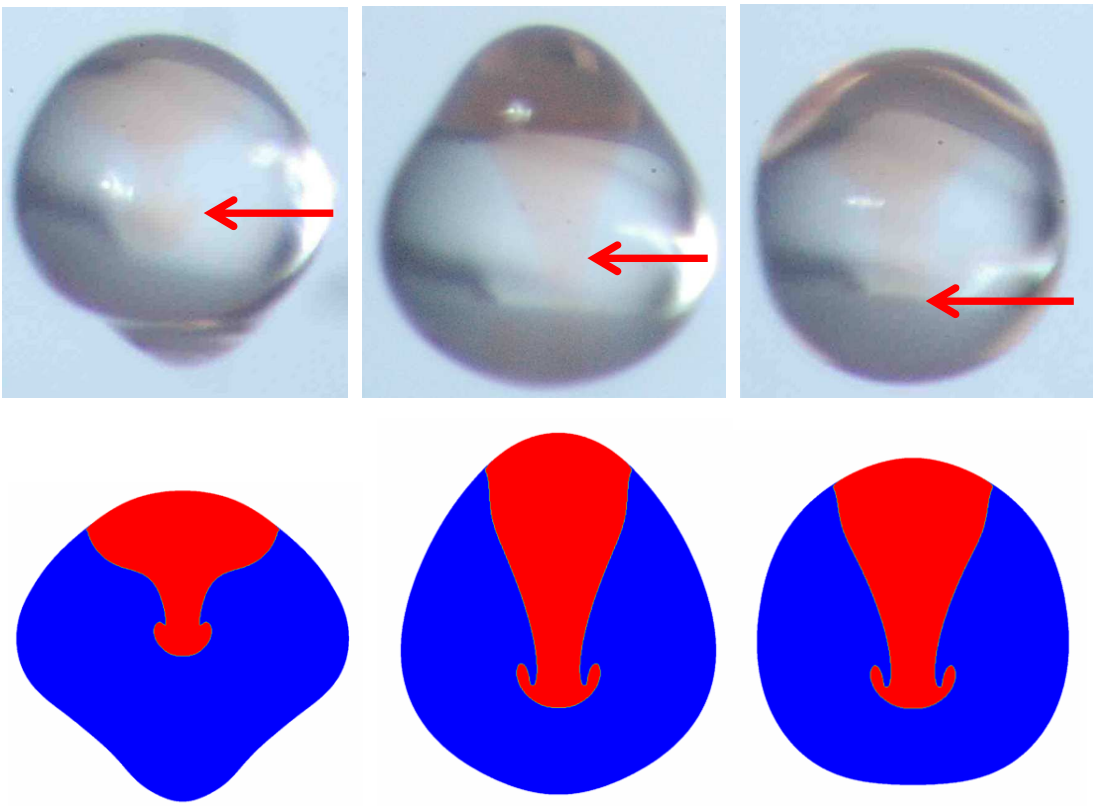

Figure 8. Enlarged images (the last three in the first column of Figure 7) show the internal jet during the collision of n-decane droplets for the case (We_S=0.84, Δ=2.03, We*=0.15).

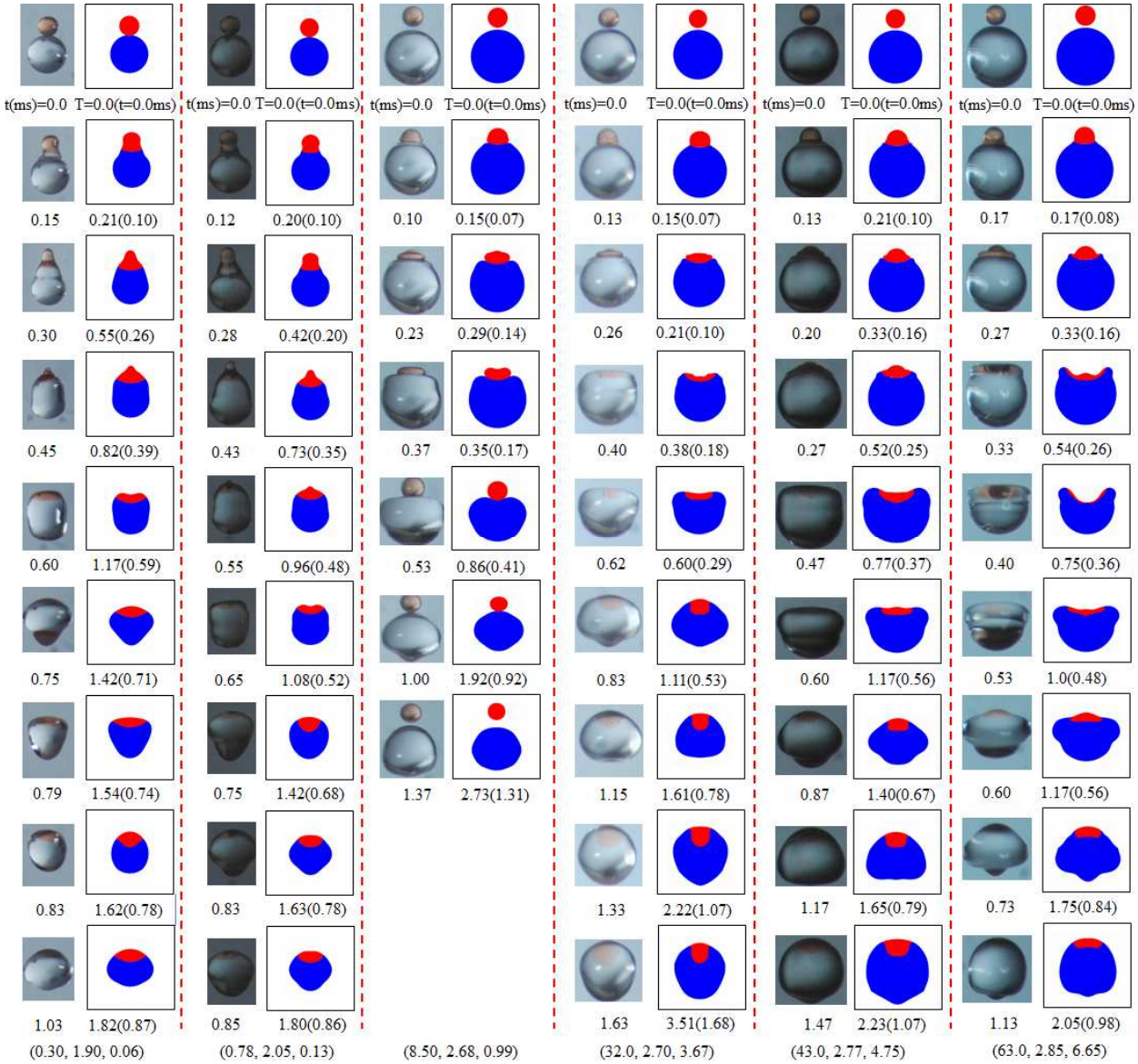

Figure 9. Mixing pattern during collision of n-tetradecane droplets for (We_S, Δ, We*). The oscillation time and the Ohnesorge number of the smaller droplet are t_{OSC}=0.48ms and Oh=0.82, respectively.

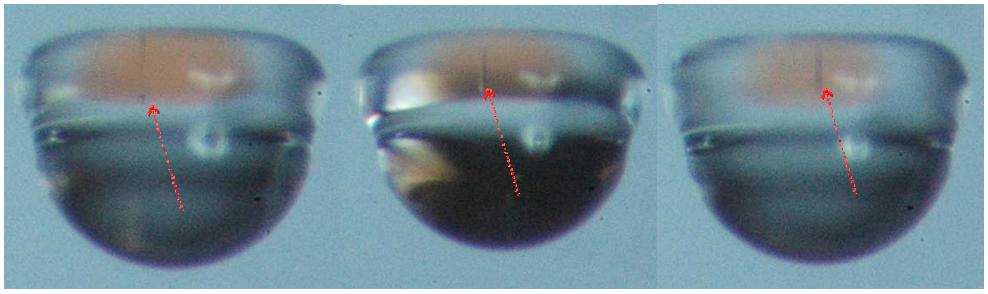

Figure 10 Gas charge entrapment during collision of n-tetradecane droplets for $We_S \approx 63.0$, $\Delta = 2.85$ at $t \approx 0.5 \pm 0.1$ms.

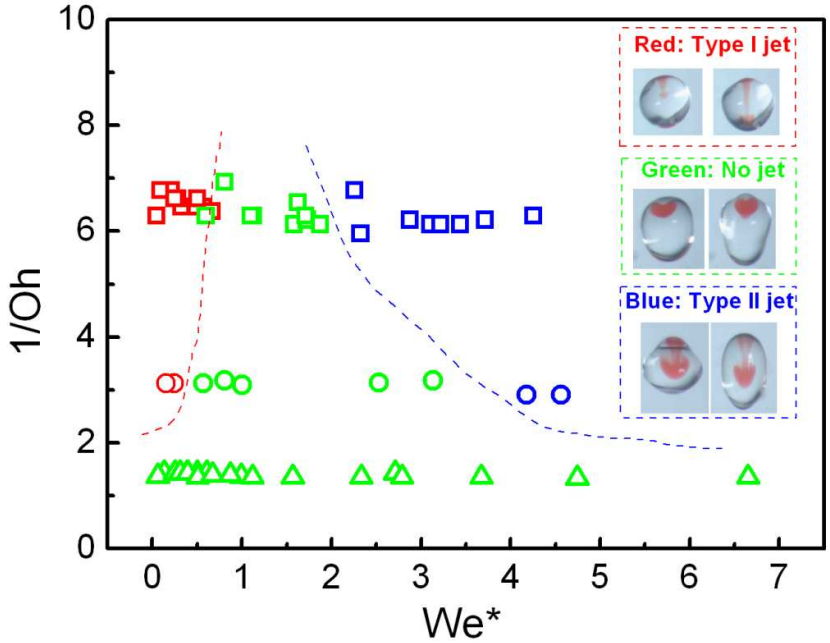

Figure 11. Regime nomogram for mixing pattern upon droplet coalescence. Open squares: water; open circles: n-decane; open triangles: n-tetradecane.

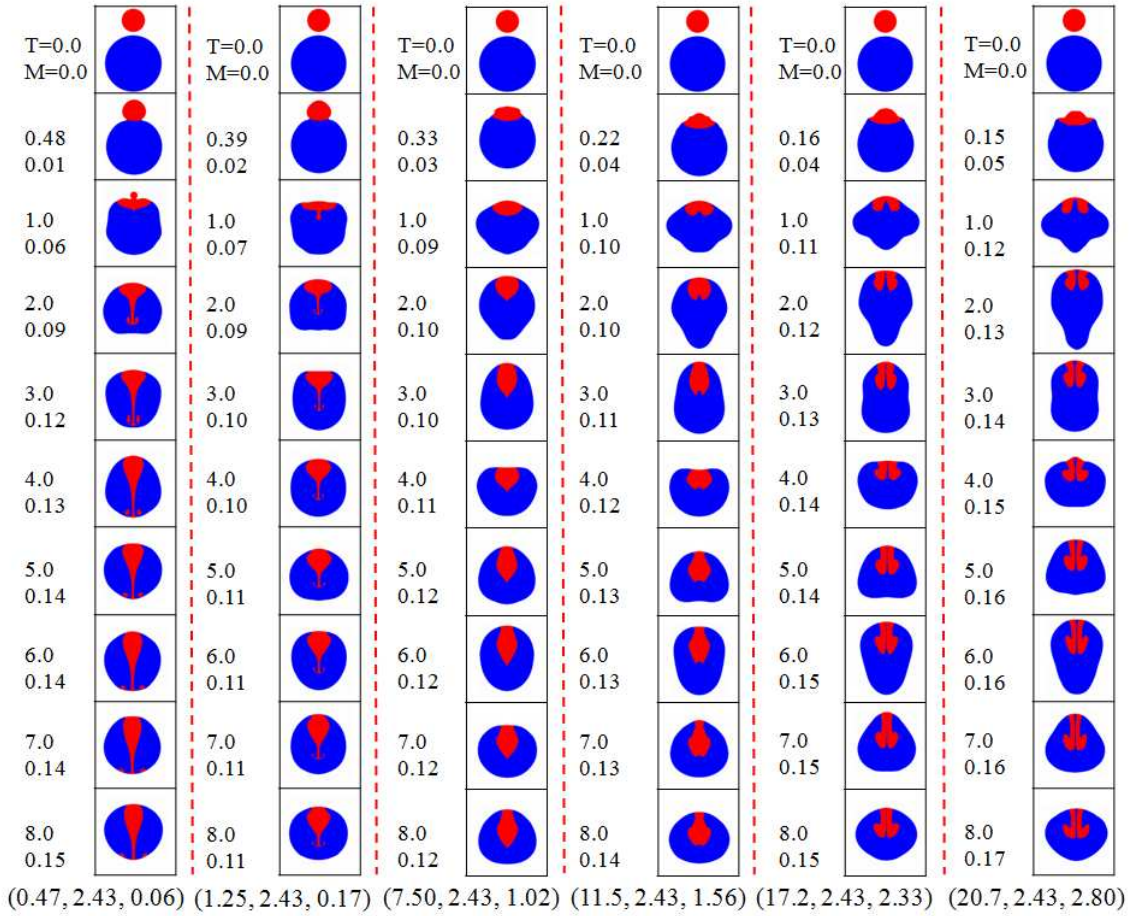

Figure 12. Calculated mixing pattern during collision of water droplets for (We_S, Δ=2.43, We*). Oh=0.19, t_{OSC}=0.33ms.

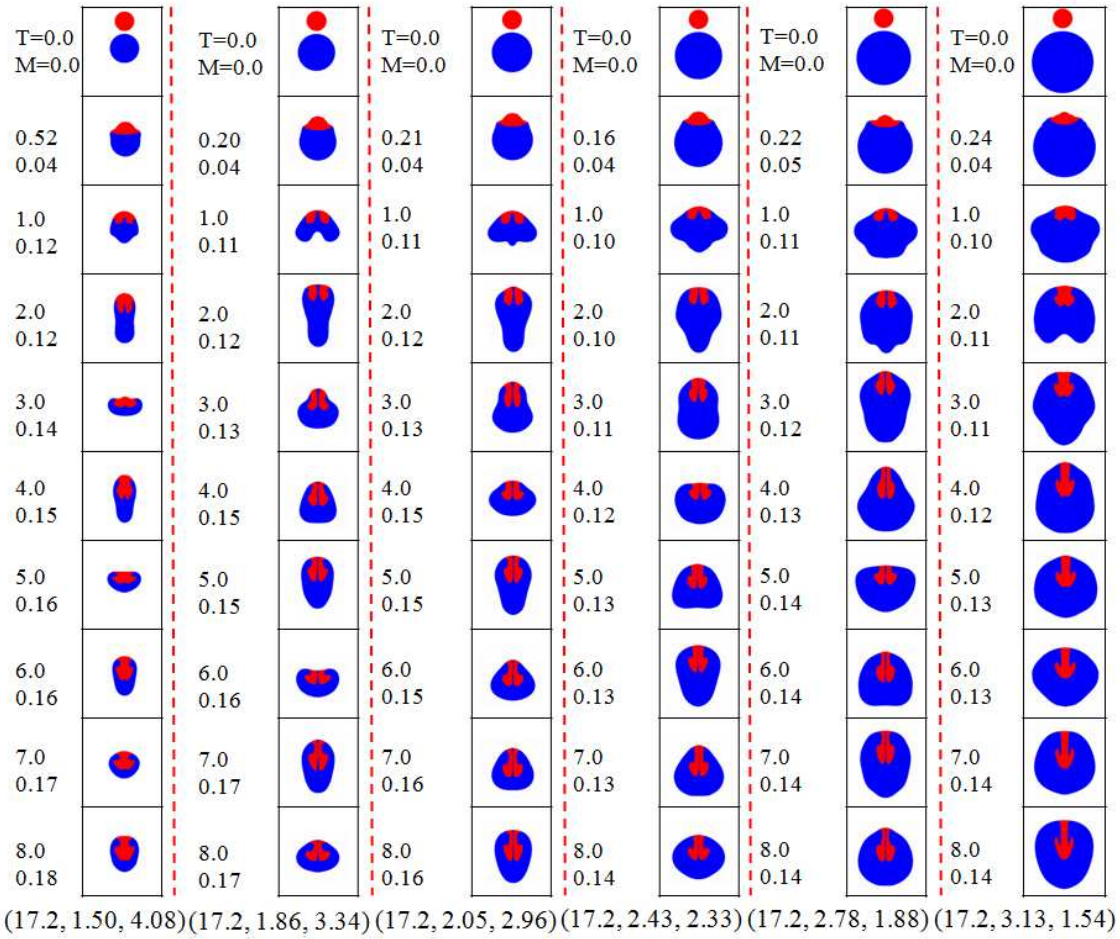

Figure 13. Calculated mixing pattern during collision of water droplets for (We_S=17.2, Δ, We*). Oh=0.19, t_{OSC}=0.33ms.

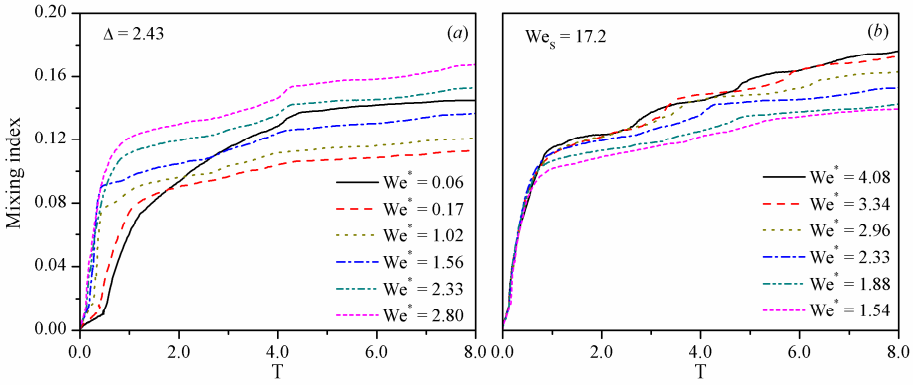

Figure 14 Mixing index for the cases in Figures 12 and 13.